International Journal of Heat and Mass Transfer 250 (2025) 127320

Contents lists available at ScienceDirect

International Journal of Heat and Mass Transfer

journal homepage: www.elsevier.com/locate/ijhmt

Enhanced pool boiling of Novec-7100 using nano/micro structured surfaces

Yu-Qing Tang [a], Xiao-Jun Hu [b], Zhan-Jun Wang [b], Cheng-Hui Sun [a], Wen-Zhen Fang [a], Wen-Quan Tao [a,*]

[a] Key Laboratory of Thermo-Fluid Science and Engineering of MOE, School of Energy and Power Engineering, Xi'an Jiaotong University, Xi'an, Shaanxi 710049, China
[b] China Information Technology Designing & Consulting Institute Co., Ltd., Beijing 100048, China

ARTICLE INFO

Keywords:
Pool boiling
Structured surface
Heat transfer coefficient
Critical heat flux
Fluorinated liquid

ABSTRACT

Fluorinated dielectric liquids (e.g., Novec-7100) are critical for electronics cooling applications, for which engineered surface textures can dramatically improve pool boiling performance. This study presents a systematic comparison between two distinct surface engineering approaches: (1) nanostructured surfaces created via chemical vapor deposition and (2) microstructured surfaces fabricated using porous copper foam and copper mesh. Through controlled pool boiling experiments, the results showed that the introduction of micro and nanostructured surfaces effectively reduced the wall superheat at the onset of nucleate boiling due to the coupling between surface structure and bubble evolution, with microstructured surfaces improving heat transfer coefficient and critical heat flux by 61.9 % and 65.23 %, respectively, which is superior to the nanostructured surfaces due to the improvement in the liquid replenishment. The three-dimensional interconnected pore structure of copper foam provides optimal cavity sizes for bubble nucleation while simultaneously enhancing liquid replenishment through capillary action. High-speed visualization reveals that copper mesh surfaces exhibit 2-fold higher bubble departure frequency than plain surfaces, directly correlating microstructural features with enhanced bubble dynamics. These findings establish porous metallic structures with multiscale porosity as the optimal solution for maximizing both heat transfer coefficient and critical heat flux in dielectric fluid boiling applications. The study advances fundamental understanding of structure-performance relationships in phase-change heat transfer and offers practical surface engineering solutions for next-generation electronics cooling systems.

1. Introduction

With the rapid advancement of cloud computing, the significant enhancement in data transmission speed greatly escalates the power consumption and heat generation of data center servers when handing massive amount of data [1–6]. As reported by Uptime Institute [7], the average power consumption per rack in 2010 was within 4–5 kW, but reached 20 kW in 2018, approaching the maximum air-cooling capacity. The latest data reported in 2022 showed that 50 % of data centers consume the power of 50 kW or even higher per rack. The increase in the power consumption poses a challenge for the heat dissipation. There is an urgent heat dissipation demands for the development of compact and efficient solutions to maintain system stability and optimize overall energy efficiency [8–13].

For the thermal management techniques, the two-phase immersion cooling method stands out prominently due to its excellent heat dissipation capabilities [14–18], where the equipment is entirely immersed in a dielectric liquid, utilizing phase change of liquids to absorb the heat. This approach realizes higher heat transfer performance, and thus reduces chip temperature [19,20]. The fluorinated liquid is highly favored for its outstanding dielectric performance, good chemical stability, and thermal transport capabilities, making it a promising medium for direct immersion cooling system [21]. It is reported that 3M™ Novec series holds a distinct advantage over 3M™ Fluorinert series [22,23] because of the significantly lower global warming potential (GWP) and zero ozone depletion potential (ODP). The performance of immersion cooling essentially depends on the pool boiling induced by the heat-generating modules, such as the CPU, GPU, etc. Therefore, an understanding of pool boiling is crucial for the design and optimization of the immersion cooling systems [24–27].

To meet the growing demand of heat dissipation, many researchers are seeking ways to further enhance the critical heat flux (CHF) values and boiling heat transfer performance of fluorinated liquids, aiming to

* Corresponding author.
E-mail address: wqtao@mail.xjtu.edu.cn (W.-Q. Tao).

https://doi.org/10.1016/j.ijheatmasstransfer.2025.127320
Received 12 February 2025; Received in revised form 11 April 2025; Accepted 25 May 2025
Available online 2 June 2025

Nomenclature

p_c	capillary pressure
k	permeability
q	heat flux
T_w	wall temperature
k_{Cu}	conductivity of copper
T_1	temperature of point 1
T_2	temperature of point 2
T_3	temperature of point 3
T_{sat}	saturation temperature
ΔT	wall superheat
Δx	interval of the rod points
h	heat transfer coefficient
U	uncertainty
c_{pl}	specific heat
r	latent heat of liquid
ρ_l	density of saturated liquid
ρ_v	density of vapor
η_l	viscosity of liquid
R_b	radius of bubble
Δp	pressure difference
T_b	saturation vapor temperature
f	bubble departure frequency

Greek symbols

φ	receding contact angle
β	inclined angle of surface
α	half-center angle

Abbreviation

CHF	critical heat flux
HTC	heat transfer coefficient
PPI	number of pores per inch
GWP	global warming potential
ODP	ozone depletion potential
SEM	scanning electron microscope
ONB	onset of nucleate boiling

address thermal management issues of high-energy density electronic components. Recently, developing new surface technologies and materials to enhance pool boiling heat transfer and improving CHF and heat transfer coefficient (HTC), is currently the focus of research [28–39]. To this end, the studies primarily focused on decorating the heating surfaces from the following three aspects: microporous structured surfaces, nanostructured surfaces and different wettability surfaces.

For the pooling boiling of fluorinated liquids on microporous structured structures, Manetti et al. [40] adopted the nickel and copper metal foam to enhance pool boiling, achieving a much higher HTC 12.4 kW/(m^2•K) compared with regular surfaces. Jiang et al. [41] conducted a comparative study on sintered copper powder and sintered copper mesh microporous surfaces, indicating that the pool boiling heat transfer performance on the microporous coated surface was significantly higher than that on polished copper surfaces. Besides, they demonstrated that the cooper mesh surface of sintered 300 in^{-1} exhibited the best performance, with a CHF of 48.95 W/cm^2 and the corresponding HTC of 22 kW/(m^2•K). Amir et al. [42] studied the performance of composite extended copper microporous surfaces that can effectively reduce the peak temperature of chip surface.

For enhanced surfaces the pooling boiling of fluorinated liquids on nanostructured surfaces, Souza et al. [43] explored the nucleate boiling phenomena of Novec-7100 with nanostructured surfaces, emphasizing the potential of nanostructure in enhancing nucleate boiling heat transfer performance. The experimental results indicated that rougher surfaces were associated with a higher HTC due to an increased number of nucleation sites. Sahu et al. [44] studied the pool boiling of Novec-7300 on copper surfaces covered with electroplated copper nanofibers, achieving the both higher CHF and HTC. Doran et al. [45] explored the impact of increasing the surface area of nanostructured surfaces on boiling performance through a combination of experiments and analytical models. Experimental results showed slightly degraded pool boiling performance from the nanostructured samples relative to the baseline samples. Cao et al. [46] modified copper surfaces using Cu-Zn (~100 nm) nanoparticles via electrophoretic deposition, and found that compared with smooth surfaces, the HTC on modified surfaces was increased by up to 100 %, while the maximum wall superheat was about 20 K lower than that of smooth surfaces, while the CHF did not show significant improvement.

In the study focusing on surfaces with different wettability

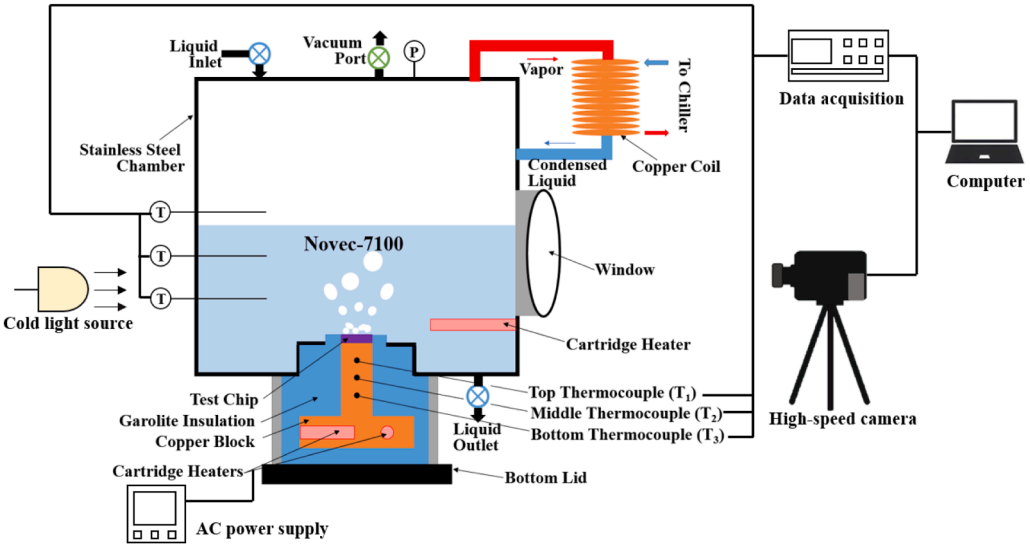

Fig. 1. Experimental setup for pool boiling.

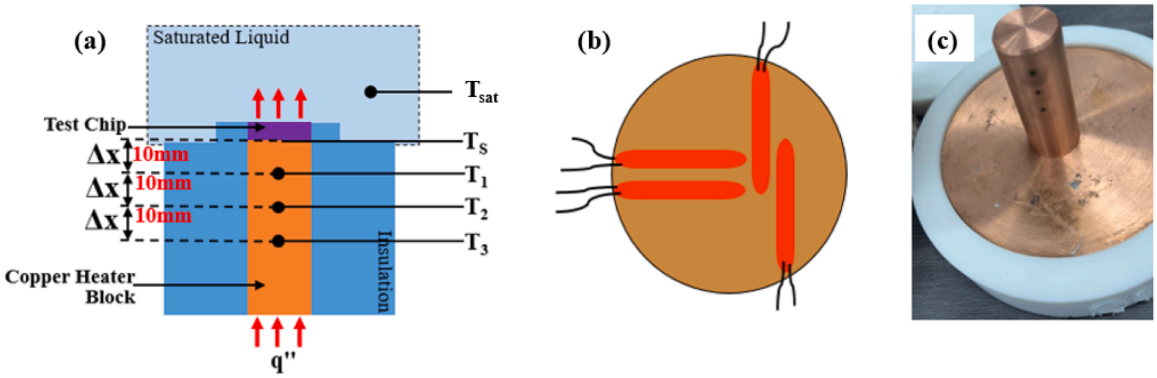

Fig. 2. Heating elements of experimental system: (a)distribution of temperature monitor positions; (b) arrangement of heating rods; (c) photograph of the heating element.

characteristics, Matic et al. [47] employed fluorosilane for surface hydrophobization to enhance pool boiling performance of Novec-649. It showed that the application of this coating did not exhibit hydrophobicity towards dielectric fluids and only slightly increased the contact angle. However, they found that the HTC reached a maximum of 13 kW/(m^2•K), which was a 54 % increase compared with the untreated surface, and the CHF was not impacted in either structured surface.

In summary, the surface modified techniques can be employed to enhance the pool boiling CHF and HTC of fluorinated liquids. However, it remains unclear which specific scale (micro or nano) of structures on surfaces is more effective in promoting the pool boiling heat transfer performance of fluorinated liquids, and the interaction between surface structures and bubble birth, growth and detachment is not yet well understood, with a lack of systematic experimental validation. In this study, pool boiling experiments of Novec-7100 were conducted on three kinds of surfaces with nanostructure, copper foam and mesh microporous structures, revealing the relationships between micro-nano structures and bubble evolution based on bubble dynamics, which effectively improved the boiling heat transfer performance of fluorinated liquids.

2. Experimental methods

2.1. Experimental setup

An experimental platform for pool boiling of Novec-7100 was built, as shown in Fig. 1, which mainly consists of four parts: heating section, chamber section, steam cooling section, and data acquisition section. The main body of the chamber is made of stainless steel, with a diameter and height of 30 cm and 20 cm, respectively. There are four windows (φ=156 mm) around the chamber for observing the motions of bubble. To maintain a stable pressure inside the chamber, the generated vapor steam is condensed back into the chamber after exchanging heat with the cooling plate on the top of chamber. The liquid temperature was maintained at saturation conditions using a 600 W auxiliary cartridge heater immersed in the working fluid. Two calibrated K-type thermocouples, positioned at 10 mm and 30 mm below the liquid surface, provided real-time temperature feedback for manual power adjustment of the heating element. The heating system effectively offset both thermal losses through the transparent chamber walls and energy dissipation due to vapor formation. Experimental measurements confirmed the liquid temperature stability within ±0.5 °C of the desired saturation point (61 °C for Novec-7100 at atmospheric pressure). Vertical temperature profiling using multiple sensors demonstrated consistent thermal uniformity, with maximum spatial variations not exceeding ±0.8 °C across the fluid volume. Temperature of the fluorinated liquids and heating elements are recorded using Keysight equipment. A high-speed camera and a cold light source are used to capture the bubble dynamics.

Table 1
Thermophysical properties of Novec-7100 under normal pressure and temperature conditions.

Property	Novec-7100
Surface tension (N/m)	0.0136
Liquid density (kg/m^3)	1510
Vapor density (kg/m^3)	9.58
Liquid viscosity (kg/(m•s))	3.61×10^{-4}
Latent heat of vaporization (kJ/kg)	112
Specific heat (J/(kg•K))	1183
Thermal conductivity (W/(m•K))	0.069
Saturation temperature (K)	61
Molecular weight (g/mol)	250

The design of the heating element made up of a copper rod is shown in Fig. 2. The copper rod has a height of 65 mm and a diameter of 25 mm. To ensure a one-dimensional heat conduction along the axis of copper rod, the polytetrafluoroethylene and alumina-silicate ceramic fiber are used around the heating components for insulation, as shown in the blue part of Fig. 2(a). To calculate the heat flux along the axis of copper rod, three temperature monitor points, T_1, T_2, and T_3, are sequentially located on the copper rod, with an interval of 10 mm. The position of T_1 is also 10 mm away from the top surface of the copper rod, as shown in the orange part of Fig. 2(a). Three T-type thermocouples with a diameter of 1 mm are used to record the variation of temperature. The bottom heating plate with a diameter of 120 mm and a thickness of 30 mm, as shown in Fig. 2(b), is made up of copper with four heating rods (diameter 6 mm × height 50 mm, rated voltage and power of 220 V and 200 W, respectively) buried inside. The uneven heating rod arrangement in Fig. 2(b) was designed to concentrate heat flux toward the copper disk center while accommodating spatial constraints. The product of heating element is shown in Fig. 2(c). During the experiment, a thermal grease with the thermal conductivity > 0.671W/(m•K) is filled in the gap between the heating components and the sample to reduce the thermal contact resistance.

The cooling liquid used in the experiments is Novec-7100, with the GWP of 297 significantly lower than that of the FC series [48]. Its thermophysical properties of Novec-7100 under the normal pressure and temperature conditions (1 atm, 25 °C) are listed in Table 1. Note that, the surface tension, thermal conductivity, and specific heat are 72.8 mN/m, 0.59 W/(m·K) and 4220 J/(kg•K) for water, respectively, while those parameters are much higher than those of Novec-7100, with 13.6 mN/m, 0.069 W/(m•K) and 1183 J/(kg•K), respectively. These dielectric fluids with a low surface tension has a strong wetting property, delaying the formation of bubbles.

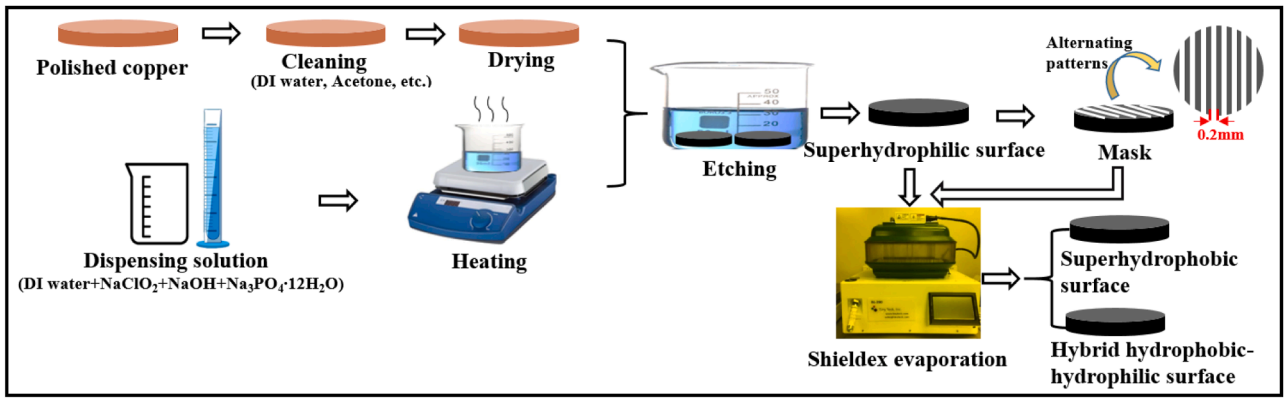

Fig. 3. Preparation of surfaces with nanostructures.

2.2. Experimental procedure

The experimental procedure began by filling the test chamber with Novec-7100 dielectric fluid to a level of 6 cm above the test surface. Following established degassing protocols, the system was maintained boiling for half an hour to ensure complete removal of dissolved non-condensable gases.

With the degassing process completed, the main heating power was systematically increased in controlled increments. Throughout the testing sequence, the fluid temperature was maintained at saturation conditions using the auxiliary heaters. At each heat flux level, the system was allowed to stabilize until steady-state conditions were achieved, defined as less than ±0.5 °C variation in surface temperature within 3 min. High-speed imaging at 1000 frames per second captured the bubble dynamics once steady-state was confirmed.

The experiment proceeded until the onset of CHF conditions, identified by the abrupt temperature rise (>10 K/s). Considering the safety, the input power was immediately reduced to 20 % of maximum upon CHF detection to protect the test surface. The collected data from multiple experimental runs were used to construct boiling curves characterizing the relationship between wall superheat and heat flux for each surface configuration.

2.3. Preparation of surfaces

The main focus of this study is to investigate the pool boiling performance of the Novec-7100 on the nanostructured surfaces prepared by chemical etching and micro-structured surfaces made up of copper mesh or copper foam.

2.3.1. Nanostructured surfaces

Studies on water pool boiling have shown that hydrophobic surfaces are favor to the bubble generation, while hydrophilic regions can improve the ability of water replenishment to increase CHF [49–51]. Thus, the hybrid hydrophobic-hydrophilic surface is proposed to improve the boiling heat transfer of water. Therefore, to investigate whether the hybrid hydrophobic-hydrophilic surfaces are also applied to Novec-7100, we fabricated superhydrophobic and hybrid hydrophobic-hydrophilic surfaces using the preparation procedure illustrated in Fig. 3.

To begin with, the surfaces are sequentially placed in solutions such as deionized water, acetone, and isopropanol, and then cleaned thoroughly using an ultrasonic bath, to remove organic substances and contaminants. Subsequently, the solution prepared with NaClO, NaOH, and $Na_3PO_4 \bullet 12H_2O$ is heated to 90 °C, and the surfaces are immersed in this solution for chemical etching to generate the nanostructure on surfaces. Finally, all the surfaces are immersed in chemical vapor

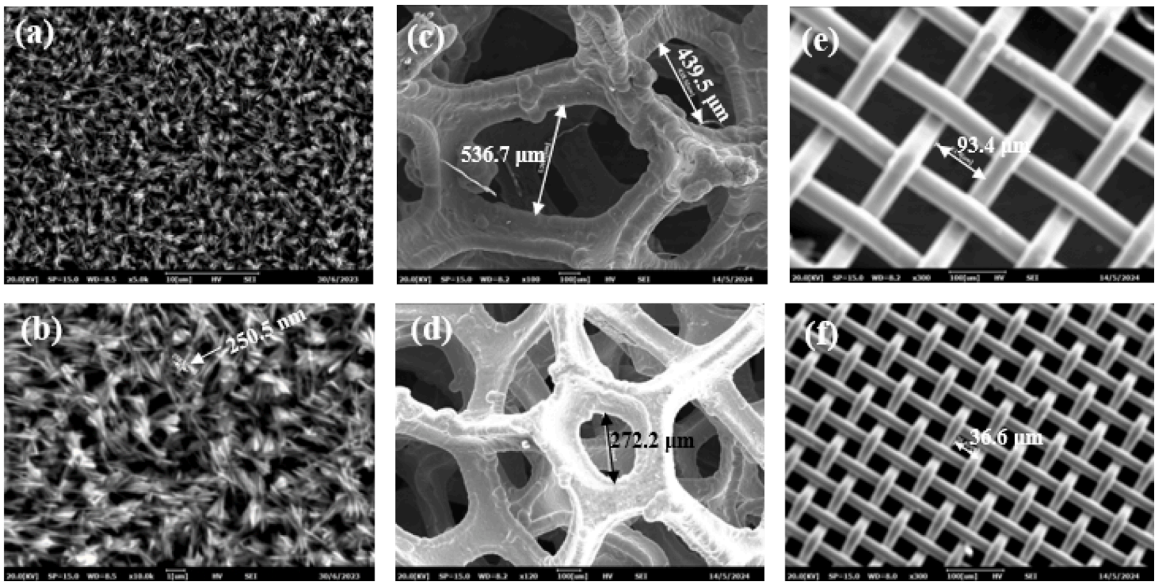

Fig. 4. SEM image of test surfaces: (a) superhydrophobic surface; (b) magnified view of the superhydrophobic surface; (c) 40 ppi copper foam; (d) 60 ppi copper foam; (e) 150 in^{-1} copper mesh; (f) 250 in^{-1} copper mesh.

deposition (CVD) system for Shieldex coating, rendering the surface to be superhydrophobic. The hybrid hydrophobic-hydrophilic surfaces with alternating wettability were fabricated through a selective coating process where photoresist-masked 0.2 mm wide stripes maintained the original hydrophilic properties, while the unmasked regions were rendered superhydrophobic via Shieldex chemical vapor deposition. As illustrated in Fig. 3, this precisely controlled patterning created periodic 0.2 mm wide alternating superhydrophilic and superhydrophobic stripes across the surface.

2.3.2. Microstructured surfaces

In this study, porous microstructured surfaces are used as the sample for the investigation of pool boiling performance on microstructured surfaces. The 150 in^{-1} copper mesh, 250 in^{-1} copper mesh and different number of pores per inch (PPI) of copper foam (40/60 PPI) were bonded to the surfaces. The PPI value is a key characteristic that distinguishes different porous materials, with higher PPI values indicating smaller pore sizes. Capillary pressure p_c and permeability k are the primary factors influencing the boiling behaviors of porous structures. The smaller the pore size, the greater the capillary pressure and the smaller the permeability. Generally, the greater capillary pressure and permeability are more favorable for enhancing the pool boiling heat transfer behaviors.

2.3.3. SEM images of surfaces

In order to better analyze the influence of different structured surfaces on bubble dynamics from the perspective of microscopic, the test surfaces are characterized using the scanning electron microscope (SEM). Fig. 4(a) depicts the SEM image of superhydrophobic surface, and its magnified view is shown in Fig. 4(b), which exhibited a needle-like structure, with a needle tip width of approximately 250.5 nm. Fig. 4 (c) and 4(d) are images of 40 ppi and 60 ppi copper foam, respectively, showing that the pore size of 40 ppi is larger than that of 60 ppi, with average pore sizes of approximately 488.1 μm and 272.2 μm, respectively. Fig. 4(e) and 4(f) are SEM images of 150 in^{-1} and 250 in^{-1} copper mesh, with the average pore sizes of 93.4 μm and 36.6 μm, respectively.

2.4. Computation simplification and uncertainty analysis

In the pool boiling experiment, to evaluate the phase change heat transfer performance of different surfaces, it is necessary to calculate the heat flux q and the wall temperature T_w of the boiling surfaces. The heat flux q can be calculated according to the one-dimensional heat conduction law:

$$q = -k_{Cu}\frac{dT}{dx}, \tag{1}$$

where the thermal conductivity of copper k_{Cu} is 387 W/(m•K). The temperature gradient along the axis of copper rod can be approximately calculated by:

$$\frac{dT}{dx} = \frac{-3T_3 + 4T_2 - T_1}{2\Delta x}. \tag{2}$$

Similarly, T_w can be obtained from T_1 and q using Eq. (3). Thus, the wall superheat ΔT is calculated as the difference between T_w and the saturation temperature T_{sat} of Novec-7100:

$$T_w = T_1 - q\left(\frac{\Delta x}{k_{cu}}\right), \tag{3}$$

$$\Delta T = T_w - T_{sat}. \tag{4}$$

The average heat transfer coefficient (HTC) of surface is determined by:

$$h = \frac{q}{\Delta T}. \tag{5}$$

In this experiment, the errors introduced by direct measurements, including temperature, length, and thermal conductivity measurements, result in uncertainties of ±0.2 K, ±0.05 mm and ±8 W/(m•K) (~2 % error), respectively. The uncertainties for physical quantities calculated from indirect measurements is determined as follows:

$$U_p = \sqrt{\sum_{i=1}^{n}\left(\frac{\partial p}{\partial \sigma_i}U_{\sigma i}\right)^2}. \tag{6}$$

Substituting the expression of q from Eq. (1) into Eq. (6) yields

$$\frac{U_q}{q} = \sqrt{\frac{(U_{k_{Cu}})^2}{k_{Cu}^2} + \frac{(U_{\Delta x})^2}{\Delta x^2} + \frac{9(U_{T_3})^2}{\alpha^2} + \frac{16(U_{T_2})^2}{\alpha^2} + \frac{(U_{T_1})^2}{\alpha^2}}, \tag{7}$$

where the coefficient $\alpha = 3T_3–4T_2+T_1$.

Similarly, the uncertainties of T_w, ΔT, and h can be derived as expressed in Eqs. (8–10) respectively:

$$\frac{U_{T_w}}{T_w} = \sqrt{\left[\frac{U_{T_1}}{\left(T_1 - q\left(\frac{\Delta x}{k_{Cu}}\right)\right)}\right]^2 + \left[\frac{U_q}{\left(\frac{k_{Cu}}{\Delta x}T_1 - q\right)}\right]^2 + \left[\frac{U_{\Delta x}}{\left(\frac{k_{Cu}}{q}T_1 - \Delta x\right)}\right]^2 + \left[\frac{U_{k_{Cu}}}{\left(\frac{k_{Cu}}{q\Delta x}T_1 - 1\right)}\right]}, \tag{8}$$

$$\frac{U_{\Delta T}}{\Delta T} = \sqrt{\left(\frac{U_{T_w}}{T_w - T_{sat}}\right)^2 + \left(\frac{U_{T_{sat}}}{T_w - T_{sat}}\right)^2}, \tag{9}$$

$$\frac{U_h}{h} = \sqrt{\left(\frac{U_q}{q}\right)^2 + \left(\frac{U_{T_w}}{T_w - T_{sat}}\right)^2 + \left(\frac{U_{T_{sat}}}{T_w - T_{sat}}\right)^2}. \tag{10}$$

3. Results and discussion

3.1. Pooling boiling on polished surfaces

In order to ensure that the data provided by pool boiling experimental platform are reliable, and to conduct comparative analysis with different structured surfaces, a study on a polished copper surface (with a diameter of 25 mm and thickness of 2 mm) was first carried out. In the experiment, the copper surface was polished repeatedly with sandpaper at first. The next step was to change the heat flux and record the surface temperature. Subsequently, the calculated h was compared and analyzed against the theoretical model proposed by Rohsenow [52]. The expression of Rohsenow formula is as follows

$$\frac{c_{pl}\Delta T}{r} = C_{wl}\left[\frac{q}{\eta_l r}\sqrt{\frac{\sigma}{g(\rho_l - \rho_v)}}\right]^{0.33}\left(\frac{c_{pl}\eta_l}{\lambda_l}\right)^s, \tag{11}$$

where, c_{pl} is the specific heat, and r is the latent heat of liquid. C_{wl} is a

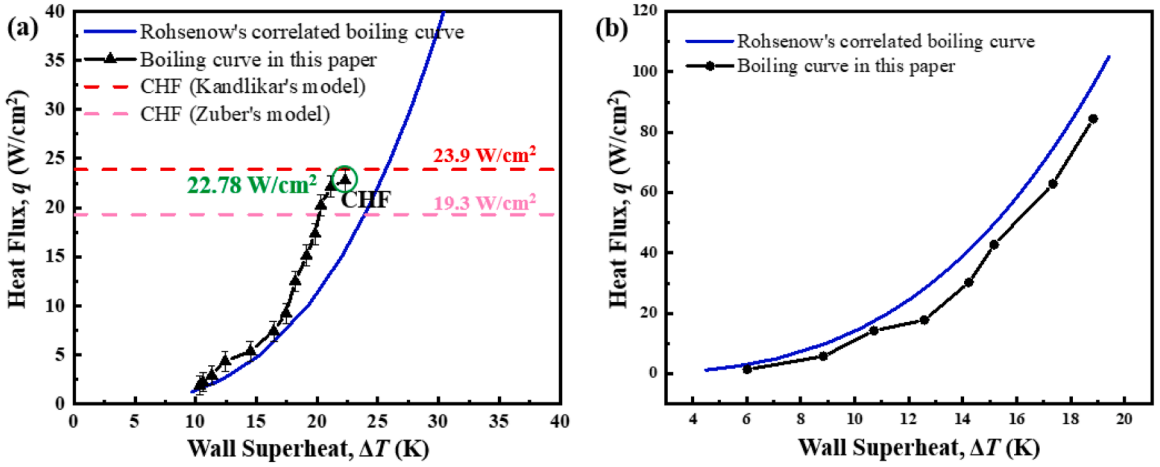

Fig. 5. The test results were compared with the correlation curves of Rohsenow and Kandlikar equations by different working fluids: (a) Novec-7100; (b) water.

coefficient depending on the combination of surface and liquid. ρ_l is the density of saturated liquid. ρ_v is the density of vapor. $s = 1.7$ for Novec-7100 and η_l is the viscosity of liquid.

For predicting CHF, the commonly adopted empirical models are proposed by Kandlikar [53] and Zuber [54]. They are respectively represented by Eq. (12) and Eq. (13):

$$q_{\mathrm{CHF}} = h_{lv}\rho_v^{\frac{1}{2}}\left(\frac{1+\cos\varphi}{16}\right)\left[\frac{2}{\pi}+\frac{\pi}{4}(1+\cos\varphi)\cos\beta\right]^{\frac{1}{2}}[\sigma g(\rho_l-\rho_v)]^{\frac{1}{4}}, \tag{12}$$

$$q_{\mathrm{CHF}} = 0.149 r\rho_v^{1/2}[\sigma g(\rho_l-\rho_v)]^{1/4}, \tag{13}$$

where φ is the receding contact angle, which is 8.32° for Novec-7100 [48]; and β is the inclined angle of surface, which is 0°.

By substituting the physical properties of Novec-7100 and water into the above three well-known pool boiling related formulas (Eqs. (11–13)), the performance of pool boiling on polished surfaces can be obtained, which are then compared with the experimental results, as shown in Fig. 5.

The calculated CHF by Kandlikar and Zuber models are 23.9 W/cm^2 and 19.3 W/cm^2 for Novec-7100 respectively, which agree well with the experimental result 22.78 W/cm^2, validating the accuracy and reliability of the experimental platform in measuring pool boiling performance. It can be observed from Fig. 5(a) that, under the same heat flux conditions, the values of ΔT obtained from experimental measurements are generally lower than those calculated from the theoretical model, with the average deviation of 11 %.

While, for the water, the average deviation for ΔT is 11.9 % in Fig. 5 (b). Note that, the CHF of water reaches 100 W/cm^2 much higher than that of Novec-7100, which is due to the higher thermal conductivity of water relative to Novec-7100. Additionally, the wall superheat for the onset of nucleate boiling (ONB) is approximately 5 K for water, while approximately 10 K for Novec-7100. To explain this phenomenon, we conduct the force and thermal balance analysis for the vapor bubble surrounded by liquid. According to the force balance condition, the pressure difference inside and outside the bubble should be balanced by the surface tension acting on the gas-liquid interface, which is described by the Laplace equation:

$$\Delta p = \frac{2\sigma}{R_b} \tag{14}$$

where Δp is the required pressure difference for the bubble of radius R_b.

Then, using Clausius-Clapeyron equation, the required superheat ΔT for a bubble of radius R_b can be obtained by:

$$T_b - T_{sat} = \frac{2\sigma T_{sat}}{r\rho_v R_b} \tag{15}$$

where T_b denotes the saturation temperature of the vapor inside the bubble, and T_{sat} denotes the referenced saturation temperature under experimental conditions. ρ_{v} and R_{b} are the vapor density and radius of vapor bubble. For the polished surfaces, the wall temperature T_{w} can be reasonably approximated as T_b. This approximation enables Eq. (15) to analyze the required wall superheat for generating bubbles of identical diameter using different working fluids. Calculations based on the above equation show that, the required ΔT to generate bubbles of the same radius for Novec-7100 is approximately 2 times that of water, which is consistent with experimental observations.

3.2. Pool boiling on nanostructured surfaces

To explore the pooling boiling behaviors of Novec-7100 on the nanostructured surfaces, we compare their performances on three different nanostructured surfaces: polished copper (S0), superhydrophobic surfaces (S1), and hybrid hydrophilic-hydrophobic surfaces (S2). At first, the contact angles of Novec-7100 on these three surfaces are measured. Note that although the superhydrophobic surface (S1) exactly shows a contact angle of 167.5° for water (shown as Fig. 6

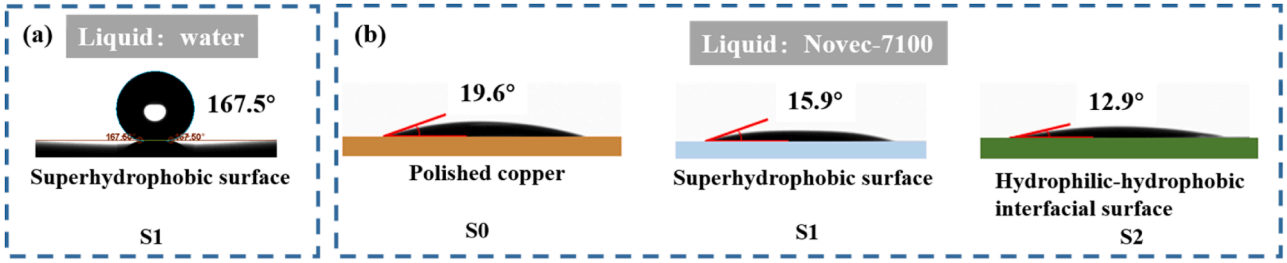

Fig. 6. Contact angle measurements: (a) water on superhydrophobic surface; (b) Novec-7100 on three kinds of surfaces.

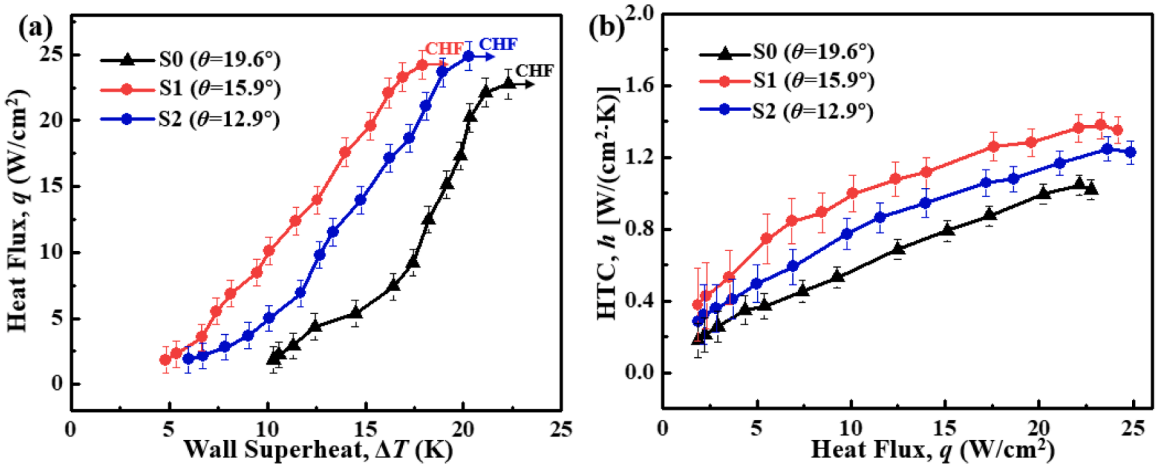

Fig. 7. The boiling curves for different nanostructured surfaces.

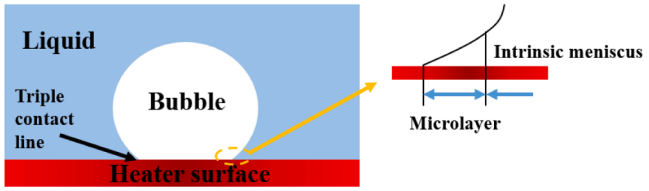

Fig. 8. Bubble morphology on heater surface showing microlayer and meniscus.

(a)), it does not work for Novec-7100 due to the low surface tension. The average contact angles of Novec-7100 on S0, S1 and S2 surfaces are 19.6°, 15.9° and 12.9°, respectively (shown as Fig. 6(b)). Due to the existence of nanostructure on S1 and S2 surface, their contact angles are lower than that of Novec-7100 on polished copper.

The dependence of heat flux on the wall superheat (ΔT) for the above three surfaces is shown in Fig. 7(a). It is observed that the value of ΔT of the ONB for the S1 and S2 surfaces are 4.85 K and 5.63 K, respectively, which is much lower than that for the S0 surface. It is because the nanostructured surfaces exhibit denser cavities for nucleation, which significantly reduce ONB. Wettability is a key factor affecting pool boiling heat transfer performance. Due to the reduction of contact angle of Novec-7100 on the nanostructured surface, the replenishment of liquid is enhanced, resulting in a slight increase in CHF compared with the polished surface. Moreover, the spatial organization of wetting properties and surface structures also dominate boiling performance. The smooth S0 surface suffers from limited nucleation sites, while the superhydrophobic S1′s needle-like nanostructures promote higher nuclear site density. Additionally, S2′s precisely patterned 0.2 mm hydrophilic-hydrophobic stripes simultaneously enable efficient liquid replenishment through hydrophilic pathways and organized vapor escape via hydrophobic zones, achieving higher CHF than S1 despite their similar contact angles.

Besides, superhydrophobic surface has a higher heat transfer coefficient h, as shown in Fig. 7(b). For example, when $q = 12.38$ W/cm^2, the HTC is 0.67 W/(cm^2·K) for the S0 surface. In contrast, the HTC is increased to 1.07 W/(cm^2·K) and 0.89 W/(cm^2·K) for surfaces S1 and surfaces S2, respectively, indicating a significant enhancement in heat transfer. The superficial explanation is that the liquid is more disturbed by the higher nucleation site density on nanostructured surfaces. While hybrid wettability-patterned surfaces S2 typically performs better than superhydrophobic surfaces S1 in conventional pool boiling, our experiments with Novec-7100 reveal an inverse trend due to some coupled mechanisms. The dielectric fluid's ultralow surface tension (13.6 mN/m) and inherent high wettability (contact angle <20°) diminish the benefit of hydrophilic patterning. Additionally, S1′s nanostructures enhance nucleation site density and bubble departure frequency (110 Hz vs 100 Hz for S2) through optimized vapor trapping, as quantified by high-speed imaging. This fluid-specific behavior, validated through bubble dynamics analysis, suggests that nanostructured superhydrophobic surfaces may be preferable for low-surface-tension dielectric fluids, whereas hybrid patterning excels mainly in high-surface-

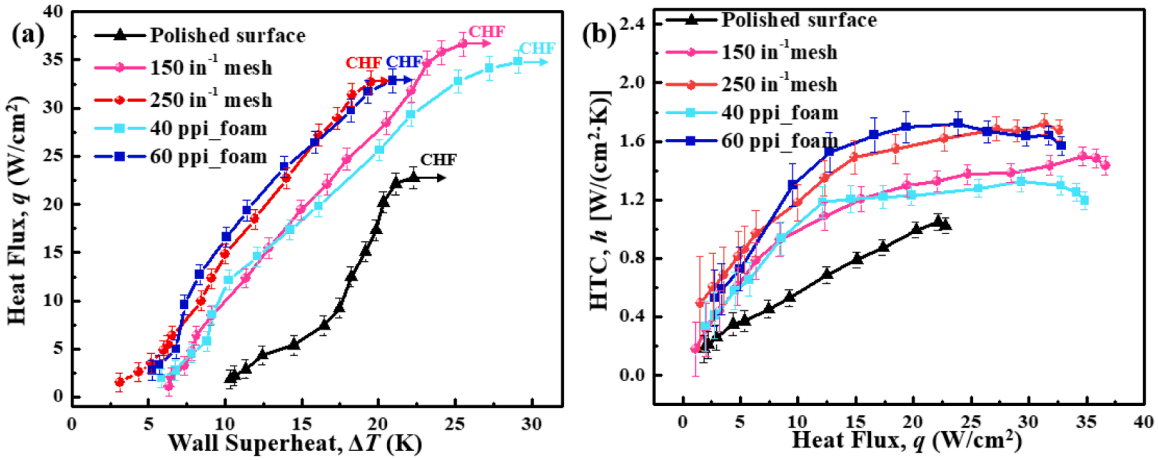

Fig. 9. The experimental results for different microstructured surfaces:(a) boiling curves; (b) relationship between HTC and q.

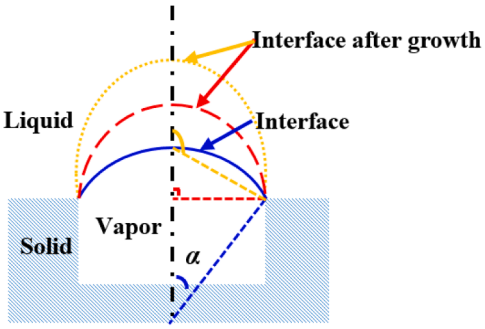

Fig. 10. Schematic diagram of the bubble growth on the micro-pore.

tension liquids like water.

For further explain the mechanism of enhanced heat transfer, many recent studies can be cited. It has been demonstrated that microscale heat transfer mechanisms play more important roles than the enhanced convection by the bubble motion [55–57]. The evaporation process at a single bubble's interface occurs primarily in two distinct zones (Fig. 8): the intrinsic meniscus zone governed by macroscopic force equilibrium, and the ultrathin microlayer adjacent to the three-phase contact line. As the microlayer is very thin, the thermal resistance between the heater surface and the vapor-liquid interface becomes negligible. Consequently, area-specific evaporation rates in the microlayer substantially exceed those in the meniscus zone. Nanostructured surfaces that expand the microlayer area while minimizing its thickness prove effective for nucleate boiling heat transfer.

3.3. The pool boiling on microstructured surfaces

This study investigates pool boiling performance of Novec-7100 on four representative microstructured surfaces: 150 in^{-1} and 250 in^{-1} copper mesh, as well as 40 ppi and 60 ppi copper foam. The boiling heat transfer performances of Novec-7100 on these four microstructured surfaces are shown in Fig. 9.

From Fig. 9(a), it can be observed that all tested microstructured porous surfaces reduce the ΔT of the ONB. For microporous surfaces, nucleation sites have been activated at the heat flux of ~1.53 W/cm^2 and wall superheat of ~5 K, which is comparable to the nanostructured surfaces and much lower than that of polished surfaces. This is because the porous structures on surfaces are suitable for the bubble nucleation, thus allowing for a lower ONB compared with polished surfaces. Microporous surface has abundant pore structures and substantial internal surface areas, which significantly increase the number of potential nucleation sites. A higher ratio of surface area per unit volume enables more molecules to adsorb at the interfaces, thereby enhancing the nucleation probability. Notably, the porous structure is particularly suitable for bubble nucleation, as its microscopic cavities can trap gas, serving as stable nucleation sites that lower the energy barrier for bubble formation. Furthermore, the porous surfaces can serve as substrates for heterogeneous nucleation, effectively reducing the critical free energy required for nucleation. Additionally, within micrometer-sized pores, high wick ability promotes liquid enrichment, thereby triggering nucleation. The interconnected pore structure facilitates rapid energy transport, mitigating nucleation delays caused by diffusion limitations.

For the polished surfaces, the wall temperature T_w can be reasonably approximated as T_b. This approximation enables Eq. (15) to analyze the required wall superheat for generating bubbles of identical diameter using different working fluids. However, for the surfaces with micro-pores, the bubble growth process can be characterized as illustrated in Fig. 10 shown below. By the half-center angle α that reaches 90°, at which the bubble curvature attains its maximum and the maximum T_b is achieved. The maximum T_b for different micro-pores exhibits an inverse dependence on the pore diameter.

The experimental investigation by Liu et al. [58] revealed that when the micro-pore diameter reaches or exceeds 75 μm, the wall temperature at ONB exceeds the maximum T_b, meaning bubble growth is possible in the heat transfer-controlled stage, with pressure equilibrium achieved before the bubble extends beyond the micro-pore. Thus, when the diameter reaches or exceeds 75 μm, the conventional monotonic decreasing relationship between wall temperature at the onset of nucleate boiling (ONB) and pore diameter no longer holds under these conditions. The most pore sizes of microstructured surfaces in our research are exceeds 75 μm, therefore the conventional inverse relationship between nucleation superheats and pore radius cannot be established under these conditions.

Microporous surfaces exhibit higher wickability, enhancing liquid supply to the heated regions [59,60], reducing the risk of drying out, and thus results in a higher CHF than that of the nanostructured surfaces and polished surfaces. Due to the higher porosity and permeability on 150 in^{-1} copper mesh compared with that of 250 in^{-1} copper mesh, the replenishment capability is better for 150 in^{-1} copper mesh, resulting in the CHF being 15.25 % and 65.23 % higher than that of surface 250 in^{-1} and the polished surfaces, respectively. Similarly, the CHF of 40 ppi copper foam surface exhibits a 6.09 % and 52.99 % improvement over surface 60 ppi and the polished surface, respectively.

As for the HTC, it can be improved by 61.9 % and 60.95 % for the 250

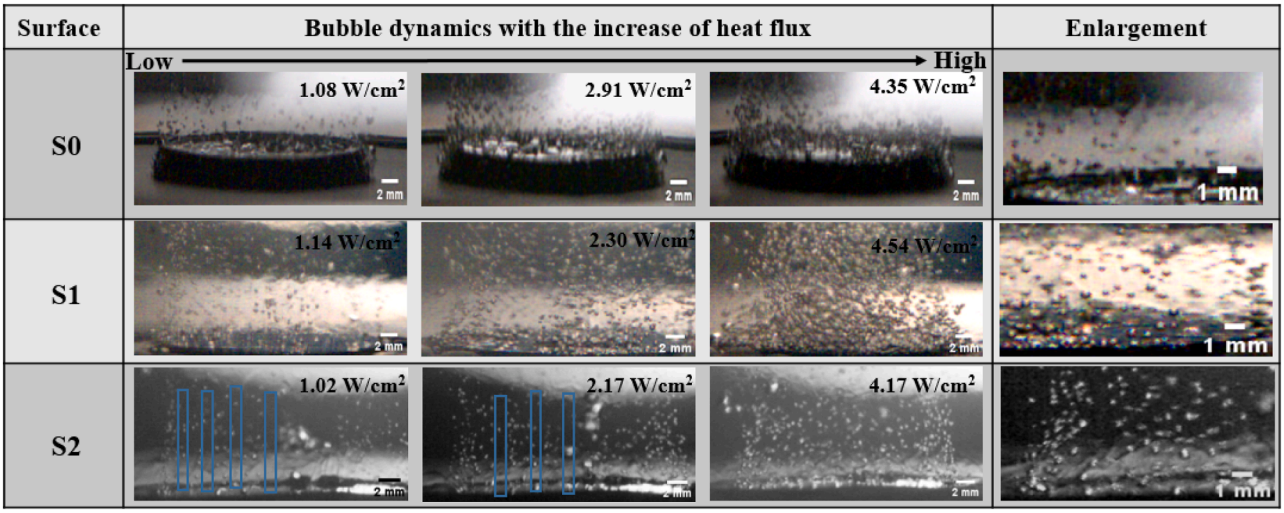

Fig. 11. Bubble dynamics captured by high-speed cameras on S0, S1 and S2 with the increase of heat flux.

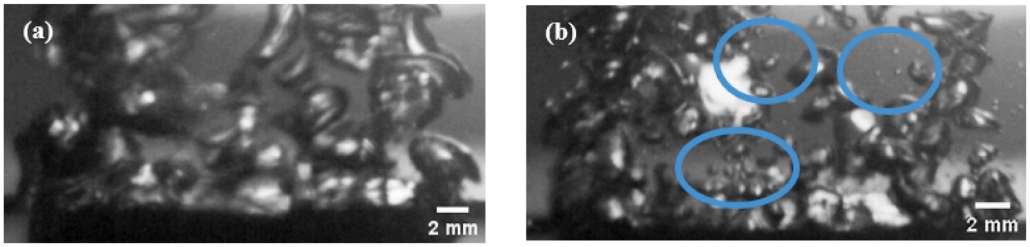

Fig. 12. Bubble columns under high heat flux situation: (a) polished surface; (b) modified surface.

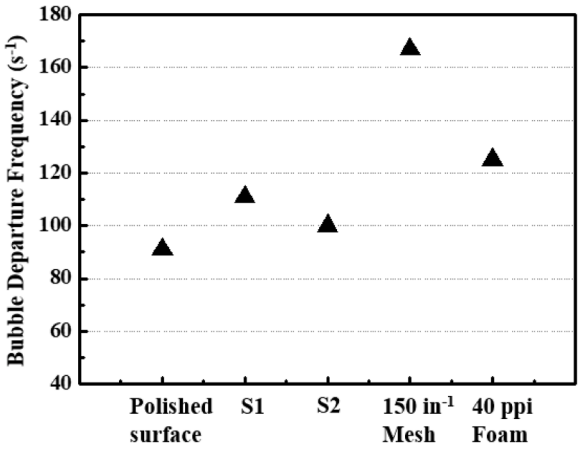

Fig. 13. Bubble departure frequency for different surfaces.

in^{-1} copper mesh and 60 ppi copper foam relative to the polished surface, respectively, as shown in Fig. 9(b). A smaller pore size corresponding to a larger specific surface area leads to the increase of nucleation sites, making their HTCs higher than those of 150 in^{-1} copper mesh and 40 ppi copper foam. Note that, when the heat flux is higher than a threshold value ~22 W/cm^2, the HTC of 60 ppi copper foam shows a decreasing trend with the heat flux. Such threshold value is lower than that of 40 ppi copper foam because of the weaker replenishment capability. Consequently, the HTC decreases when the heat flux exceeds the threshold one, where a low thermal conductivity of vapor tends to cover the surfaces.

3.4. Bubble dynamics behaviors

3.4.1. Bubble nucleation site density

As obtained using a high-speed camera, the images of the bubble dynamics at three different heat-flux intervals of the nanostructured surfaces are shown in Fig. 11. Simultaneously, the bubble behavior under the second heat flux condition was magnified here. At high heat flux, the aggregation of vapor bubbles complicates the observation of bubble dynamics. Conversely, at lower heat flux (in the isolated bubble regime), the high-speed camera can effectively capture the processes of bubble formation, growth, and detachment. Therefore, bubble observation was conducted at the heat fluxes of approximately 1 W/cm^2 to 4 W/cm^2.

Compared with the polished surface, the nanostructured surfaces provide more nucleation sites for the bubble formation. Additionally, on the S2 surface where hybrid hydrophilic-hydrophobic regions exist, since the contact angle of Novec-7100 on the hydrophilic region is smaller than that on hydrophobic region, it is more difficult to generate bubbles on the hydrophilic region. Consequently, during the initial stage of boiling, the non-bubble zones corresponding to the hydrophilic regions appear, as indicated in the blue box in Fig. 11. Similar to the nanostructured surfaces, the introduction of the two kinds of microstructured surfaces, copper mesh and copper foam, significantly increase the number of nucleation sites, thereby greatly enhancing the boiling heat transfer coefficient. Due to the similarity between the microporous structures and the bubble detachment diameters (approximately 0.4 mm), it is easier to form stable nucleation sites and achieve lower ONB.

Table 2
CHF and HTC of different surfaces and their improvement compared with polished surfaces.

Test surfaces	CHF (W/cm^2)	CHF improvement	Maximum HTC [W/(cm^2•K)]	HTC improvement
Polished surface	22.78	/	1.05	/
150 in^{-1} mesh	37.64	65.23 %	1.44	37.14 %
250 in^{-1} mesh	32.66	43.37 %	1.70	61.90 %
40 ppi foam	34.85	52.99 %	1.30	23.81 %
60 ppi foam	32.85	44.21 %	1.69	60.95 %
S1	24.21	6.28 %	1.38	31.43 %
S2	24.90	9.31 %	1.25	19.05 %

With the increase of heat flux, bubbles on the surface begin to aggregate before detaching from the surface, forming the bubble column, as illustrated in Fig. 12. However, some small isolated bubbles can still be observed on the modified surfaces until reaching CHF, as shown in Fig. 12(b).

3.4.2. Bubble departure frequency

The high-speed camera is used to record the entire process of bubble generation, growth, and eventual departure from the heated surface. The bubble departure frequency f is defined as the number of bubble cycles occurring per unit of time at a specific cavity location [61]. At a heat flux of approximately 2 W/cm^2, the bubble departure frequencies of various modified surfaces are shown in Fig. 13. Compared with polished surfaces, microporous surfaces provide more nucleation sites due to trapped residual gases in their cavities and pores. However, the higher bubble departure frequency primarily results from smaller bubble departure sizes and faster bubble growth rates. In the initial phase, bubble expansion is governed by inertial forces, with fast vaporization being the dominant mechanism. Later, it transitions to a heat-transfer-controlled regime, where the porous structure enhances local heat flux, accelerating vapor generation. The constrained pore morphology prevents bubble coalescence while encouraging the generation of smaller bubbles, which demonstrates increased detachment rates under the influence of both buoyancy and inertial forces.

During the initial stages of boiling, the presence of residual gases promotes rapid bubble formation, leading to increased bubble coverage on the surface. This enhanced interaction between the liquid and bubbles improves heat transfer efficiency. Even though both are microstructured surfaces, there is a significant difference in bubble departure frequency in the Fig. 13. This discrepancy is due to the thickness of the copper mesh being 0.2 mm, while the copper foam has a thickness of 2.5

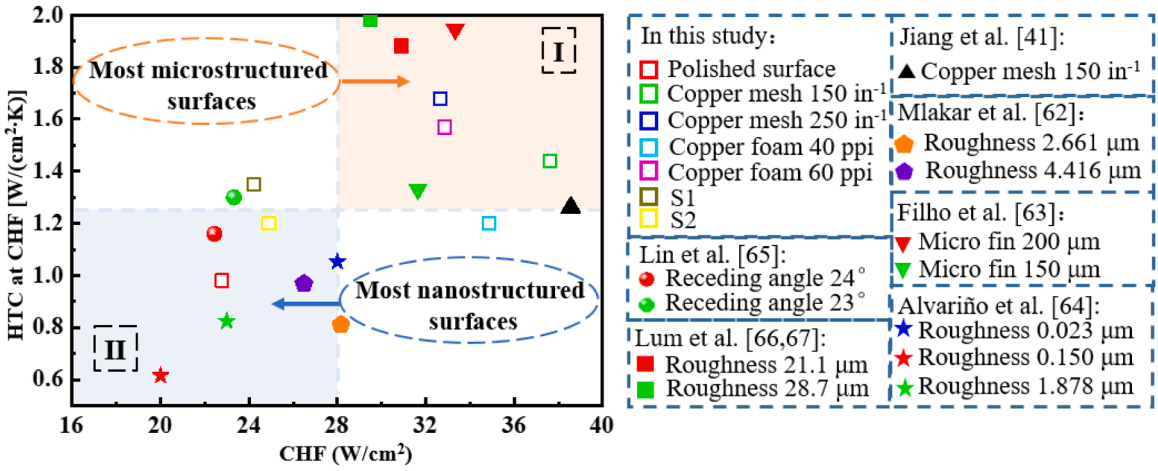

Fig. 14. CHF and HTC of Novec-7100 on different structured surfaces from literatures.

Table 3
A literature review on methods to enhance the pool boiling of Novec-7100 in recent years.

References	Publication year	Processing method	Surface structure	CHF (W/cm^2)	HTC at CHF [W/(cm^2•K)]
This study	/	CVD	Nano needle.	24.21	1.35
This study	/	Bonding	Micro pores	32.66	1.68
[47]	2022	Sintering	Copper mesh	38.56	1.26
[62]	2023	Grinding/Milling	Surface roughness	28.16	0.81
[63]	2021	Microtextured surface	Microfin array	33.33	1.95
[64]	2019	Sintering	Surface roughness	28	1.05
[65]	2024	Femtosecond laser	Microgroove	22.44	1.16
[66]	2025	Additively-manufactured	Surface roughness	28.2	1.98

mm. The increased thickness of the copper foam contributes to larger bubble evacuation resistance and a longer detachment time. Additionally, the detachment time on the nanostructured surface is not significantly improved when compared with the polished surface.

3.5. Comparison between nano and microstructured surfaces

To clearly demonstrate the influence of nanostructures and microstructures on the boiling performances of Novec-7100, in this work, we summarize the pool boiling performances of the above seven surfaces (polished surface, two nanostructured surfaces, and four microstructured surfaces), as shown in Table 2.

According to Table 2, it can be observed that the modification of surfaces all leads to an enhancement in HTC and CHF. Among them, the 250 in^{-1} copper mesh with microporous structures exhibits the highest enhancement ratio of HTC, reaching 61.9 %. However, the HTC of S2 surface with nanoporous structures only marginally increases 19.05 %. As for the CHF, the CHF of 150 in^{-1} copper mesh shows an increase of 65.23 % compared with polished surfaces, while the nanostructured surfaces only increase up to 9.31 % since they only slightly enhanced the liquid replenishment via the improved wettability for the Novec-7100.

Below, a summary of recent literature on enhancing boiling performance of Novec-7100 with different structured surfaces is provided and compared with the experimental results in this study [41,62–67], as shown in Fig. 14. The upper-right corner of figure denotes the region (Region I) with higher CHF and HTC, and thus it is the ideal approach for improving the boiling heat transfer. Whereas the lower-left region (Region II) represents areas where the enhancement of heat transfer is less pronounced. Intriguingly, we found that the structured surfaces located in Region I, such as copper mesh, copper foam, and micro-fins, generally have pore sizes of several hundred micrometers, indicative of microstructured surface design, can effectively improve the CHF and HTC simultaneously. While surfaces in Region II generally with a surface roughness of only a few hundred nanometers are not as efficient as the microstructured surfaces.

The above comparative analysis reveals that for Novec-7100 fluorinated liquid, the microstructured surface design is superior to the nanostructured surface design. Table 3 provides a detailed listing of the processing methods for the aforementioned modified surfaces and their pool boiling properties.

4. Conclusion

This study investigates the pool boiling behaviors of Novec-7100 on nanostructured and microstructured surfaces. Nanostructured surfaces contain superhydrophobic and hybrid hydrophobic-hydrophilic surfaces, while microstructured surfaces include 150 in^{-1} copper mesh, 250 in^{-1} copper mesh, 40 ppi copper foam, and 60 ppi copper foam. The main conclusions are as follows:

(1) Nanostructured and microstructured surfaces both have more nucleation sites, and can effectively reduce wall superheat of ONB compared with the polished surfaces. Specifically, compared with the polished surface, the HTC of the superhydrophobic and hydrophobic-hydrophilic surfaces increased by 31.43 % and 19.05 %, respectively. Since these nanostructured surfaces can only slightly enhance the wettability of Novec-7100, the CHF has improved marginally when compared with polished surfaces. For microstructured surfaces, 150 in^{-1} copper mesh, 250 in^{-1} copper mesh, 40 ppi copper foam, and 60 ppi copper foam, relative to polished surface, respectively increase the HTC by 37.14 %, 61.90 %, 23.81 % and 60.95 %. The CHF of these surfaces increased by 65.23 %, 43.37 %, 52.99 % and 44.21 %, respectively.

(2) Through the comparison of the nanostructured and microstructured surfaces, it was found that microstructured surfaces can attract more liquid through capillary action, increasing the replenishment of liquid, and thus significantly improving CHF.

Microstructured surfaces are superior to the nanostructured surfaces in enhancing boiling heat transfer performance of Novec-7100, thus offering crucial guidance for designing more efficient and reliable electronics immersion cooling.

CRediT authorship contribution statement

Yu-Qing Tang: Writing – original draft, Validation, Methodology, Formal analysis, Data curation, Conceptualization. **Xiao-Jun Hu:** Validation, Resources. **Zhan-Jun Wang:** Validation, Resources, Conceptualization. **Cheng-Hui Sun:** Methodology, Data curation. **Wen-Zhen Fang:** Validation, Methodology. **Wen-Quan Tao:** Writing – review & editing, Supervision, Conceptualization.

Declaration of competing interest

The authors declare that they have no known competing financial interests or personal relationships that could have appeared to influence the work reported in this paper.

Acknowledgement

This work was financially supported by the Foundation for Innovative Research Groups of the National Natural Science Foundation of China (No. 51721004), the Fund of Xi'an Science and Technology Bureau (20192187 14SYS002CG024), and the NSFC-STINT (Energy Management of Fuel Cell Powered Data Centers) (51911530157). We sincerely thank Engineer Peng He for his technical support and guidance in operating microfluidic laboratory equipment.

Data availability

Data will be made available on request.

References

[1] N. Zhang, B. Jiao, Y. Ye, Y. Kong, X. Du, R. Liu, B. Cong, L. Yu, S. Jia, K. Jia, Embedded cooling method with configurability and replaceability for multi-chip electronic devices, Energy Convers. Manage. 253 (2022) 115124.
[2] D. Zhuang, Y. Yang, G. Ding, X. Du, Z. Hu, Optimization of microchannel heat sink with rhombus fractal-like units for electronic chip cooling, Int. J. Refrig. 116 (2020) 108–118.
[3] A.M. Abbas, A.S. Huzayyin, T.A. Mouneer, S.A. Nada, Effect of data center servers' power density on the decision of using in-row cooling or perimeter cooling, Alex. Eng. J. 60 (4) (2021) 3855–3867.
[4] X. Sun, Z. Han, X. Li, Simulation study on cooling effect of two-phase liquid-immersion cabinet in data center, Appl. Therm. Eng. 207 (2022) 118142.
[5] Y. Zhang, K. Shan, X. Li, H. Li, S. Wang, Research and technologies for next-generation high-temperature data centers–State-of-the-arts and future perspectives, Renewable Sustainable Energy Rev. 171 (2023) 112991.
[6] Q. Zhang, C. Tang, T. Bai, Z. Meng, Y. Zhan, J. Niu, M.J. Deen, A two-layer optimal scheduling framework for energy savings in a data center for cyber–physical–social systems, J. Syst. Archit. 116 (2021) 102050.
[7] https://zh.uptimeinstitute.com/resources/research-and-reports.
[8] Q. Zhang, Z. Meng, X. Hong, Y. Zhan, J. Liu, J. Dong, T. Bai, J. Niu, M.J. Deen, A survey on data center cooling systems: technology, power consumption modeling and control strategy optimization, J. Syst. Archit. 119 (2021) 102253.
[9] B. Zhan, S. Shao, H. Zhang, C. Tian, Simulation on vertical microchannel evaporator for rack-backdoor cooling of data center, Appl. Therm. Eng. 164 (2020) 114550.
[10] Y. Wang, D. Nörtershäuser, S. Le Masson, J.M Menaud, Potential effects on server power metering and modeling, Wireless Networks 4 (2023) 1–8.
[11] C. Nadjahi, H. Louahlia, S. Lemasson, A review of thermal management and innovative cooling strategies for data center, Sustainable Comput. 19 (2018) 14–28.
[12] Y. Huang, B. Liu, S. Xu, C. Bao, Y. Zhong, C. Zhang, Experimental study on the immersion liquid cooling performance of high-power data center servers, Energy (2024) 131195.
[13] P. Birbarah, T. Gebrael, T. Foulkes, A. Stillwell, A. Moore, R. Pilawa-Podgurski, N. Miljkovic, Water immersion cooling of high power density electronics, Int. J. Heat Mass Transf. 147 (2020) 118918.
[14] B.B. Kanbur, C. Wu, S. Fan, F. Duan, System-level experimental investigations of the direct immersion cooling data center units with thermodynamic and thermoeconomic assessments, Energy 217 (2021) 119373.
[15] B.B. Kanbur, C. Wu, S. Fan, W. Tong, F. Duan, Two-phase liquid-immersion data center cooling system: experimental performance and thermoeconomic analysis, Int. J. Refrig. 118 (2020) 290–301.
[16] X. Yuan, X. Zhou, Y. Pan, R. Kosonen, H. Cai, Y. Gao, Y. Wang, Phase change cooling in data centers: a review, Energy Build. 236 (2021) 110764.
[17] B.B. Kanbur, C. Wu, F. Duan, Multi-criteria thermoeconomic and thermodynamic assessments of the desalination-integrated two-phase liquid-immersion data center cooling system, Int. J. Energy Res. 44 (13) (2020) 10453–10470.
[18] Y. Wang, L. Ren, Z. Yang, Z. Deng, W. Ding, Application of two-phase immersion cooling technique for performance improvement of high power and high repetition avalanche transistorized subnanosecond pulse generators, IEEE Trans. Power Electron. 37 (3) (2021) 3024–3039.
[19] S. Xu, H. Zhang, Z. Wang, Thermal management and energy consumption in air, liquid, and free cooling systems for data centers: a review, Energies 16 (3) (2023) 1279.
[20] C. Zhang, X. Sun, Z. Han, X. Li, J. Dong, Energy saving potential analysis of two-phase immersion cooling system with multi-mode condenser, Appl. Therm. Eng. 219 (2023) 119614.
[21] G. Liang, I. Mudawar, Review of pool boiling enhancement by surface modification, Int. J. Heat Mass Transf. 128 (2019) 892–933.
[22] Y.T. Hsu, J.X. Li, M.C. Lu, Enhanced immersion cooling using two-tier micro-and nano-structures, Appl. Therm. Eng. 131 (2018) 864–873.
[23] https://www.ipcc.ch/publications_and_data/ar4/wg1/en/ch2s2-10-2.html.
[24] M.S. El-Genk, Immersion cooling nucleate boiling of high power computer chips, Energy Convers. Manage. 53 (1) (2012) 205–218.
[25] C.S. Lim, G. Di Sia, Y.M. Hung, Extraordinary enhancement of nucleate pool boiling on intrinsically biphilic graphene nanostructured surfaces, Appl. Therm. Eng. 218 (2023) 119354.
[26] C. Falsetti, J. Chetwynd-Chatwin, E.J Walsh, Pool boiling heat transfer of NOVEC 649 on sandblasted surfaces, Int. J. Thermofluids 22 (2024) 100615.
[27] R. Pastuszko, R. Kaniowski, N. Dadas, Bedla-Pawlusek M. pool boiling enhancement and a method of bubble diameter determination on surfaces with deep minichannels, Int. J. Heat Mass Transf. 179 (2021) 121713.
[28] U. Sajjad, A. Sadeghianjahromi, H.M. Ali, C.C. Wang, Enhanced pool boiling of dielectric and highly wetting liquids-a review on enhancement mechanisms, Int. Commun. Heat Mass Transfer 119 (2020) 104950.
[29] R. Kaniowski, R. Pastuszko, Pool boiling experiment with NOVEC-649 in microchannels for heat flux prediction, Exp. Therm Fluid Sci. 141 (2023) 110802.
[30] P. Warrier, A. Sathyanarayana, D.V. Patil, S. France, Y. Joshi, A.S. Teja, Novel heat transfer fluids for direct immersion phase change cooling of electronic systems, Int. J. Heat Mass Transf. 55 (2012) 3379–3385.
[31] N. Tran, U. Sajjad, R. Lin, C.C. Wang, Effects of surface inclination and type of surface roughness on the nucleate boiling heat transfer performance of HFE-7200 dielectric fluid, Int. J. Heat Mass Transf. 147 (2020) 119015.
[32] G. Liang, Y. Chen, H. Yang, D. Li, S. Shen, Nucleate boiling heat transfer and critical heat flux (CHF) from micro-pit surfaces, Int. J. Heat Mass Transf. 152 (2020) 119510.
[33] B.S. Kim, S. Shin, D. Lee, G. Choi, H. Lee, K.M. Kim, H.H. Cho, Stable and uniform heat dissipation by nucleate-catalytic nanowires for boiling heat transfer, Int. J. Heat Mass Transf. 70 (2014) 23–32.
[34] M. Yuan, J. Wei, Y. Xue, J. Fang, Subcooled flow boiling heat transfer of FC-72 from silicon chips fabricated with micro-pin-fins, Int. J. Therm. Sci. 48 (7) (2009) 1416–1422.
[35] L.X. Yang, Y.M. Chao, L. Jia, C.B. Li, Wettability and boiling heat transfer study of black silicon surface produced using the plasma immersion ion implantation method, Appl. Therm. Eng. 99 (2016) 253–261.
[36] T. Emir, M. Budakli, M. Arik, Pool boiling heat transfer: thermal performance for alternating and extended operational conditions, Int. J. Heat Mass Transf. 226 (2024) 125454.
[37] R. Kibushi, K. Yuki, N. Unno, T. Ogushi, M. Murakami, T. Numata, T. Ide, H. Nomura, Enhancement of the critical heat flux of saturated pool boiling by the breathing phenomenon induced by lotus copper in combination with a grooved heat transfer surface, Int. J. Heat Mass Transf. 179 (2021) 121663.
[38] L. Wangyu, L. Zhen, L. Yuanqiang, Enhanced boiling heat transfer performance on wettability-patterned surface, Appl. Therm. Eng. (2024) 122792.
[39] Y. Shah, H.G. Kim, W.W. Choi, S.M. Kim, Experimental pool boiling study on novel multistage cross-flow porous structure using FC-72 for high-heat-flux electronic applications, Int. J. Heat Mass Transf. 213 (2023) 124270.
[40] L.L. Manetti, G. Ribatski, R.R. de Souza, E.M. Cardoso, Pool boiling heat transfer of HFE-7100 on metal foams, Exp. Therm Fluid Sci. 113 (2020) 110025.
[41] Y. Jiang, G. Zhou, J. Zhou, F. Zhou, X. Huai, Saturated pool boiling heat transfer of HFE-7100 on sintered copper powder and wire mesh microporous surfaces: a comparison study, Appl. Therm. Eng. 216 (2022) 119067.
[42] A.F. Ali, M.S. El-Genk, Spreaders for immersion nucleate boiling cooling of a computer chip with a central hot spot, Energy Convers. Manage. 53 (1) (2012) 259–267.
[43] R.R. Souza, E.M. Cardoso, J.C Passos, Confined and unconfined nucleate boiling of HFE7100 in the presence of nanostructured surfaces, Exp. Therm Fluid Sci. 91 (2018) 312–319.
[44] R.P. Sahu, S. Sinha-Ray, S. Sinha-Ray, A.L. Yarin, Pool boiling of NOVEC 7300 and self-rewetting fluids on electrically-assisted supersonically solution-blown, copper-plated nanofibers, Int. J. Heat Mass Transf. 95 (2016) 83–93.
[45] B. Doran, B. Zhang, A. Walker, K.C. Pratik, W.J. Meng, A.L. Moore, Experimental determination of the role of increased surface area in pool boiling from nanostructured surfaces, Exp. Therm Fluid Sci. 111 (2020) 109956.

[46] Z. Cao, Z. Wu, A.D. Pham, Y. Yang, S. Abbood, P. Falkman, T. Ruzgas, C. Albèr, B. Sundén, Pool boiling of HFE-7200 on nanoparticle-coating surfaces: experiments and heat transfer analysis, Int. J. Heat Mass Transf. 133 (2019) 548–560.
[47] M. Može, V. Vajc, M. Zupančič, I. Golobič, Hydrophilic and hydrophobic nanostructured copper surfaces for efficient pool boiling heat transfer with water, water/butanol mixtures and NOVEC 649, Nanomaterials 11 (12) (2021) 3216.
[48] M.H. Rausch, L. Kretschmer, S. Will, A. Leipertz, A.P. Fröba, Density, surface tension, and kinematic viscosity of hydrofluoroethers HFE-7000, HFE-7100, HFE-7200, HFE-7300, and HFE-7500, J. Chem. Eng. Data 60 (12) (2015) 3759–3765.
[49] H. Jo, H.S. Ahn, S. Kang, M.H. Kim, A study of nucleate boiling heat transfer on hydrophilic, hydrophobic and heterogeneous wetting surfaces, Int. J. Heat Mass Transf. 54 (25–26) (2011) 5643–5652.
[50] H.R. Cho, S.C. Park, D. Kim, H.M. Joo, D.I. Yu, Experimental study on pool boiling on hydrophilic micro/nanotextured surfaces with hydrophobic patterns, Energies 14 (22) (2021) 7543.
[51] H.Y. Hsu, M.C. Lin, B. Popovic, C.R. Lin, N.A. Patankar, A numerical investigation of the effect of surface wettability on the boiling curve, PLoS One 12 (11) (2017) e0187175.
[52] I.L. Pioro, Experimental evaluation of constants for the Rohsenow pool boiling correlation, Int. J. Heat Mass Transf. 42 (11) (1999) 2003–2013.
[53] S.G. Kandlikar, A theoretical model to predict pool boiling CHF incorporating effects of contact angle and orientation, J. Heat Transf. 123 (6) (2001) 1071–1079.
[54] N. Zuber, Hydrodynamic Aspects of Boiling Heat Transfer, University of California, Los Angeles, California, 1959.
[55] E.K. Dong, I.Y. Dong, W.J. Dong, H.K. Moo, S.A. Ho, Review of boiling heat transfer enhancement on micro/nanostructured surfaces, Exp. Therm Fluid Sci. 66 (2015) 173–196.
[56] S.K. Gupta, R.D. Misra, Development of micro/nanostructured-Cu-TiO2-nanocomposite surfaces to improve pool boiling heat transfer performance, Heat Mass Transfer 56 (8) (2020) 2529–2544.
[57] M. Bongarala, H. Hu, J.A. Weibel, S.V. Garimella, Microlayer evaporation governs heat transfer enhancement during pool boiling from microstructured surfaces, Appl. Phys. Lett. 120 (22) (2022).
[58] J. Liu, Q. Li, L. Liu, B. Liu, P. Zhou, Experimental study of the effect of the micro-cavity diameter on the onset of nucleate pool boiling, Int. J. Heat Mass Transf. 239 (2025) 126507.
[59] L.L. Manetti, A.S. Moita, R.R. de Souza, E.M. Cardoso, Effect of copper foam thickness on pool boiling heat transfer of HFE-7100, Int. J. Heat Mass Transf. 152 (2020) 119547.
[60] H.S. Jo, M.W. Kim, T.G. Kim, S. An, H.G. Park, J.G. Lee, S.C. James, J. Choi, S. S Yoon, Supersonically spray-coated copper meshes as textured surfaces for pool boiling, Int. J. Therm. Sci. 132 (2018) 26–33.
[61] S.J. Thiagarajan, R. Yang, C. King, S. Narumanchi, Bubble dynamics and nucleate pool boiling heat transfer on microporous copper surfaces, Int. J. Heat Mass Transf. 89 (2015) 1297–1315.
[62] G. Mlakar, C.N. Huang, C. Kharangate, Effects of surface modifications on pool boiling heat transfer with HFE-7100, Int. J. Thermofluids 17 (2023) 100286.
[63] Santos dos, E. Filho, I.S. Kiyomura, B.A. de Andrade, E.M. Cardoso, Pool boiling performance of HFE-7100 on hierarchically structured surfaces, Case Stud. Therm. Eng. 28 (2021) 101536.
[64] P.F. Alvariño, M.L. Simón, M. dos Santos Guzella, J.M. Paz, J.M. Jabardo, L. C Gómez, Experimental investigation of the CHF of HFE-7100 under pool boiling conditions on differently roughened surfaces, Int. J. Heat Mass Transf. 139 (2019) 269–279.
[65] H.C. Lin, C.H. Kang, H.C. Cheng, T.L. Chang, P.H. Chen, Saturated boiling enhancement of NOVEC-7100 on microgrooved surfaces with groove-induced anisotropic properties, Appl. Sci. 14 (2) (2024) 495.
[66] L.Y. Lum, K.C. Leong, J.Y. Ho, The synergistic effect of micro/nanostructure length scale and fluid thermophysical properties on pool boiling heat transfer, Appl. Therm. Eng. 259 (2025) 124878.
[67] L.Y. Lum, P. Liu, J.Y. Ho, Micro/nanostructuring of metal additively manufactured aluminum alloy for enhanced pool boiling of dielectric fluids, Int. J. Heat Mass Transf. 221 (2024) 125090.